

Tuning Quantum Phase Transitions at Half Filling in 3L-MoTe₂/WSe₂ Moiré Superlattices

Mingjie Zhang^{1,2}, Xuan Zhao^{1,2}, Kenji Watanabe³, Takashi Taniguchi⁴, Zheng Zhu⁵,
Fengcheng Wu^{6,7}, Yongqing Li^{1,2} and Yang Xu^{1,2,*}

¹Beijing National Laboratory for Condensed Matter Physics, Institute of Physics,
Chinese Academy of Sciences, Beijing 100190, China

²School of Physical Sciences, University of Chinese Academy of Sciences, Beijing 100049, China


³Research Center for Functional Materials, National Institute for Materials Science,
1-1 Namiki, Tsukuba 305-0044, Japan

⁴International Center for Materials Nanoarchitectonics, National Institute for Materials Science,
1-1 Namiki, Tsukuba 305-0044, Japan

⁵Kavli Institute for Theoretical Sciences and CAS Center for Excellence in Topological Quantum
Computation, University of Chinese Academy of Sciences, Beijing 100190, China

⁶School of Physics and Technology, Wuhan University, Wuhan 430072, China

⁷Wuhan Institute of Quantum Technology, Wuhan 430206, China

 (Received 27 February 2022; revised 10 August 2022; accepted 14 September 2022; published 9 November 2022)

Many sought-after exotic states of matter are known to emerge close to quantum phase transitions, such as quantum spin liquids and unconventional superconductivity. It is, thus, desirable to experimentally explore systems that can be continuously tuned across these transitions. Here, we demonstrate such tunability and the electronic correlation effects in triangular moiré superlattices formed between trilayer MoTe₂ and monolayer WSe₂ (3L-MoTe₂/WSe₂). Through transport measurements, we observe an electronic analog of the Pomeranchuk effect at half filling of the first moiré subband, where increasing temperature paradoxically enhances charge localization. At low temperatures the system exhibits the characteristic of a Fermi liquid with strongly renormalized effective mass, suggesting a correlated metal state. The state is highly susceptible to out-of-plane electric and magnetic fields, which induce a Lifshitz transition and a metal-insulator transition (MIT), respectively. It enables identification of a tricritical point in the quantum phase diagram at the base temperature. We explain the Lifshitz transition in terms of interlayer charge transfer under the vertical electric field, which leads to the emergence of a new Fermi surface and immediate suppression of the Pomeranchuk effect. The existence of quantum criticality in the magnetic-field-induced MIT is supported by scaling behaviors of the resistance. Our work shows the 3L-MoTe₂/WSe₂ lies in the vicinity to the MIT point of the triangular lattice Hubbard model, rendering it a unique system to manifest the rich correlation effects at an intermediate interaction strength.

DOI: [10.1103/PhysRevX.12.041015](https://doi.org/10.1103/PhysRevX.12.041015)

Subject Areas: Condensed Matter Physics
Strongly Correlated Materials

I. INTRODUCTION

The discovery of correlated phenomena in twisted bilayer graphene opens a new avenue for studying electron correlations in two-dimensional (2D) moiré superlattices, which host novel band structure reconstruction and exotic quantum phases [1–4]. Lately, semiconductor moiré systems based on transition-metal dichalcogenide (TMDC) heterostructures have been shown to offer alternative

platforms with appealing opportunities [5–15]. Moiré excitons, trions, and polaritons [16–22], Mott insulators [23–25], generalized Wigner crystals at fractional fillings [26–28] (including those that spontaneously break rotational symmetry [29,30]), and topological phases [31] have been experimentally observed. It is generally accepted that the low-energy Hamiltonian of the TMDC moiré system can be effectively described by the triangular lattice Hubbard model [5], which is one of the central paradigms in describing correlated systems with geometrical frustration [32–37]. When doped with one charge per site (half-filled band), the large spin entropy owing to the frustration and competing orders can give rise to the Pomeranchuk effect or an exotic nonmagnetic insulating state [e.g., quantum spin liquids (QSLs)], depending on the interaction strength U/W , where U is the on-site Coulomb repulsion

*yang.xu@iphy.ac.cn

Published by the American Physical Society under the terms of the [Creative Commons Attribution 4.0 International license](https://creativecommons.org/licenses/by/4.0/). Further distribution of this work must maintain attribution to the author(s) and the published article's title, journal citation, and DOI.

energy and W is the bandwidth [37]. Despite extensive research efforts on the triangular lattice Hubbard model, many aspects of its rich phase diagram remain unexplored due to the high complexity of the problem and the lack of suitable experimental platforms in different coupling regimes.

In TMDC moiré homo- or heterobilayers (such as twisted WSe₂ or MoTe₂/WSe₂) with small band offsets between neighboring layers, the charge density and vertical electric fields can be independently controlled by electrostatic gates, enabling *in situ* tuning across quantum phase transitions (QPTs) [38,39]. However, the precise nature of the QPT so far is not well understood [38,40–43]. The canonical problem of the Hubbard model under an external magnetic field, which can polarize the spins and control the exchange interactions, is also unsettled and worth further investigation [44–47]. Utilizing the sensitivity of the interaction strength to the dielectric environment and interlayer coupling, we fabricate a new type of moiré heterostructure consisting of trilayer MoTe₂ and monolayer WSe₂. The multilayer TMDC (3L-MoTe₂ here)-based superlattices can also potentially offer new opportunities to explore moiré physics (e.g., that arises from the Γ valley instead of the K valley) exhibiting different symmetries and strengths of spin-orbit coupling [8,48–50]. Detailed information of the band structure analyses for bare 3L-MoTe₂ and the 3L-MoTe₂/WSe₂ heterostructure is presented in Supplemental Material [51].

In this paper, we discover a rich and exotic quantum phase diagram tuned by both out-of-plane electrical and magnetic fields in the 3L-MoTe₂/WSe₂. At half filling of the first moiré subband, we find a resistance peak that counterintuitively develops with increasing temperature. This behavior resembles the Pomeranchuk effect observed in He-3 and is attributed to the close vicinity of our system to the MIT point in the triangular lattice Hubbard model. Because of the small valence band offset of the two materials, the hole-type charge carriers are first injected into the MoTe₂ and the subband population from WSe₂ can be continuously tuned by the vertical electric field, which drives a Lifshitz transition and alters the charge transport greatly. The process is accompanied by a breakdown of the single-band Hubbard model description of the system. The magnetic field, which suppresses spin fluctuations, can induce a MIT following the quantum critical scaling. We observe continuous closure of the charge gap when approaching the quantum critical point from the insulating side and divergence of effective quasiparticle mass from the metallic side.

II. METHODS

Natural trilayer MoTe₂ (2H phase) and monolayer WSe₂ flakes are mechanically exfoliated and angle aligned to form 3L-MoTe₂/WSe₂ moiré superlattices (see Supplemental Material [51] for more details). The two materials

have a lattice mismatch of about 7%, generating a maximum moiré wavelength of 5 nm and a superlattice density of approximately $5 \times 10^{12} \text{ cm}^{-2}$. The 3L-MoTe₂/WSe₂ heterostructure is encapsulated by hexagonal boron nitride sheets (about 5–10 nm thick) as gate dielectrics and patterned into a quasi-Hall bar structure [see the device schematic and an optical image in Fig. 1(a)] for electronic transport measurements. Top and bottom gate electrodes are made by few-layer graphite. Charge carriers with density n (hole type) and a vertical electric displacement field D can be introduced by the combination of top and bottom gates (V_{tg} and V_{bg} , respectively).

Transport data under in-plane magnetic fields and higher temperatures ($> 70 \text{ K}$) are acquired in a He-4 cryostat (base $T = 1.7 \text{ K}$, magnetic field B up to 9 T). All the other data are acquired in a He-3 cryostat (base $T = 300 \text{ mK}$, B up to 9 T). Measurements are performed using a standard low-frequency (9.373 Hz) lock-in technique under a small bias voltage (1–2 mV). Voltage drops V_{xx} and V_{xy} and source-drain current (I) are recorded simultaneously to obtain the corresponding longitudinal and Hall resistances. Both the voltage drops are measured using voltage preamplifiers with large input impedance (100 M Ω) to maintain the measurement accuracy. Bottom Pt electrodes (that have a large work function) and large negative top-gate bias (V_{tg}) help to obtain Ohmic hole contacts to the 3L-MoTe₂/WSe₂.

III. RESULTS

Figure 1(b) shows the longitudinal 2D sheet resistance ρ_{xx} as a function of V_{tg} and V_{bg} measured at an intermediate temperature $T = 20 \text{ K}$. The two arrows denote the directions for increasing D or n , respectively. Notably, the sample exhibits a resistance peak along a constant density line [with $n \approx 5 \times 10^{12} \text{ cm}^{-2}$; see Supplemental Fig. S1(d) [51]], corresponding to one hole per moiré unit cell or half filling of the first moiré subband, namely, moiré filling factor $\nu = 1$. We do not observe any sharp feature corresponding to the $\nu = 2$ band insulating state. Instead, the resistance exhibits a broadened hump at $V_{\text{bg}} < \sim 2 \text{ V}$ due to charge population of the Γ valley in the 3L-MoTe₂ (see more discussions in Supplemental Material [51]). Upon increasing the D field, the $\nu = 1$ peak disappears abruptly (near $D \sim 1.5 \text{ V nm}^{-1}$). The behavior is reminiscent of a recently reported bandwidth-tuned Mott transition in MoTe₂/WSe₂ heterobilayers [38]. However, we find that the resistance peak here is gradually suppressed with decreasing temperature and completely vanishes at the lowest $T = 0.3 \text{ K}$ [see the resistance color mappings and constant V_{tg} line cuts at selective temperatures in Figs. 1(c) and 1(d), respectively], in sharp contrast to the Mott insulating state [23,24,26]. In other words, the resistance peak at half filling gets enhanced only at elevated temperatures, indicating a heat-induced charge localization at the

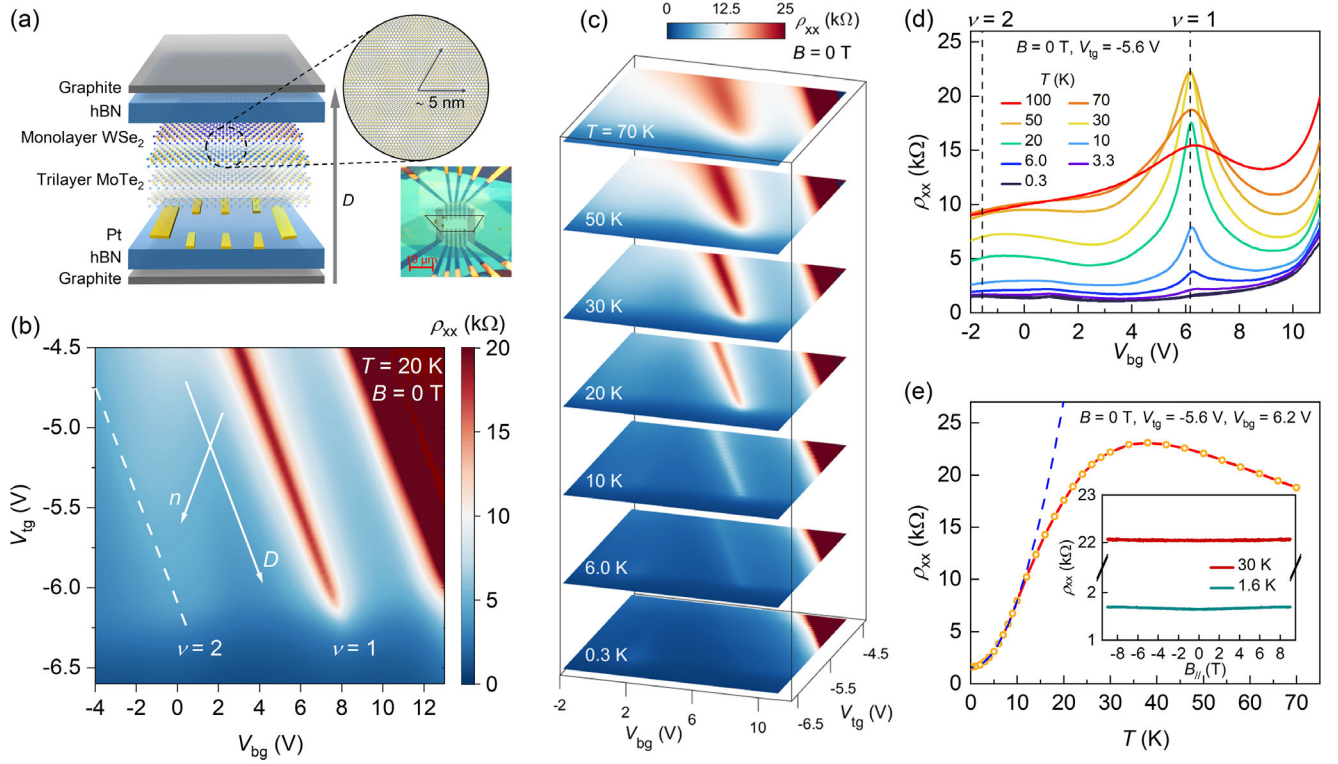


FIG. 1. Device structure and Pomeranchuk effect in 3L-MoTe₂/WSe₂ moiré superlattices. (a) Schematic (left) and optical micrograph (lower right) of the device with double graphite gates. The conduction channel of the device is outlined by the black curves in the micrograph. The scale bar is 10 μm . (b) 2D longitudinal resistance ρ_{xx} as a function of top and bottom gate voltages (V_{tg} and V_{bg} , respectively) at $T = 20$ K and zero magnetic field. An obvious resistivity peak is observed at half filling $\nu = 1$. The dashed line marks the expected position of full filling $\nu = 2$. The two arrows denote the directions of increasing D and n , respectively. (c) Evolution of ρ_{xx} as a function of T . Each color map plane shows the ρ_{xx} versus V_{tg} and V_{bg} at a fixed T . (d) The ρ_{xx} as a function of bottom gate voltage at a fixed top gate voltage $V_{tg} = -5.6$ V at different temperatures. Two dashed lines indicate the position of $\nu = 1$ and $\nu = 2$, respectively. (e) Temperature dependence and in-plane magnetic field dependence (inset) of ρ_{xx} at $V_{tg} = -5.6$ V and $V_{bg} = 6.2$ V ($\nu = 1$ and $D = 1.313$ V nm⁻¹). At low temperatures ($T < 10$ K), $\rho_{xx}(T)$ follows a Fermi liquid behavior $AT^2 + \rho_0$ (blue dashed curve).

specific commensurate doping density ($\nu = 1$). Similar effects in moiré superlattices were first reported in magic-angle twisted bilayer graphene (TBG) [52,53] and referred to as the Pomeranchuk effect, which is an electronic analog of the higher-temperature solidification of He-3 [32,37,54–56]. This unusual behavior is due to the larger spin entropy in the localized state (solid phase in He-3 or singly occupied state in 3L-MoTe₂/WSe₂). The system is then favorable to increase the degree of localization upon heating. The neighboring local moments in 3L-MoTe₂/WSe₂ have antiferromagnetic superexchange interactions [5,23,37,38], whereas in TBG isospin polarization is favored for the $|\nu| = 1$ states [52,53]. Phenomenologically, we note that a similar Pomeranchuk effect is observed in the MoTe₂/WSe₂ heterobilayers at a very narrow electric field range near the critical electric field ($E_c \sim 0.65$ V nm⁻¹) that drives the MIT [38]. However, we point out that the underlying mechanisms could be very different for the two systems (explained later).

A representative ρ_{xx} versus T curve for the $\nu = 1$ state (at $D = 1.313$ V nm⁻¹) is shown in Fig. 1(e). The sample exhibits an insulating behavior ($d\rho_{xx}/dT < 0$) at

temperatures higher than $T^* \sim 40$ K, below which a crossover to a metallic behavior ($d\rho_{xx}/dT > 0$) is observed with ρ_{xx} decreasing by more than one order of magnitude (from about 40 to 0.3 K). At $T < \sim 10$ K, the $\rho_{xx}(T)$ can be well described by a Fermi liquid behavior $\rho_{xx}(T) = AT^2 + \rho_0$ (highlighted by the dashed blue curve), where $A^{1/2}$ is proportional to the quasiparticle effective mass m^* (Kadowaki-Woods scaling) [57,58] and ρ_0 is the residual resistance. The value of A is extracted to be (64.1 ± 0.9) Ω/K^2 or (4.53 ± 0.06) $\mu\Omega\text{cm}/\text{K}^2$, considering a thickness of approximately 0.7 nm for a single layer of MoTe₂. This value is comparable to those of many heavy fermion systems, indicating substantial quasiparticle-quasiparticle scatterings and a strongly renormalized effective mass at low temperatures [59]. A maximum of $\rho_{xx} \sim 25$ k Ω is reached at $T^* \sim 40$ K, indicating $k_F l$ (with k_F being the Fermi wave vector and l being the mean free path) of the system to be about unity, as inferred from the Ioffe-Regel criteria. T^* is known as the coherence temperature characterizing the related energy scales (such as the renormalized bandwidth W^*) in strongly correlated materials [60,61].

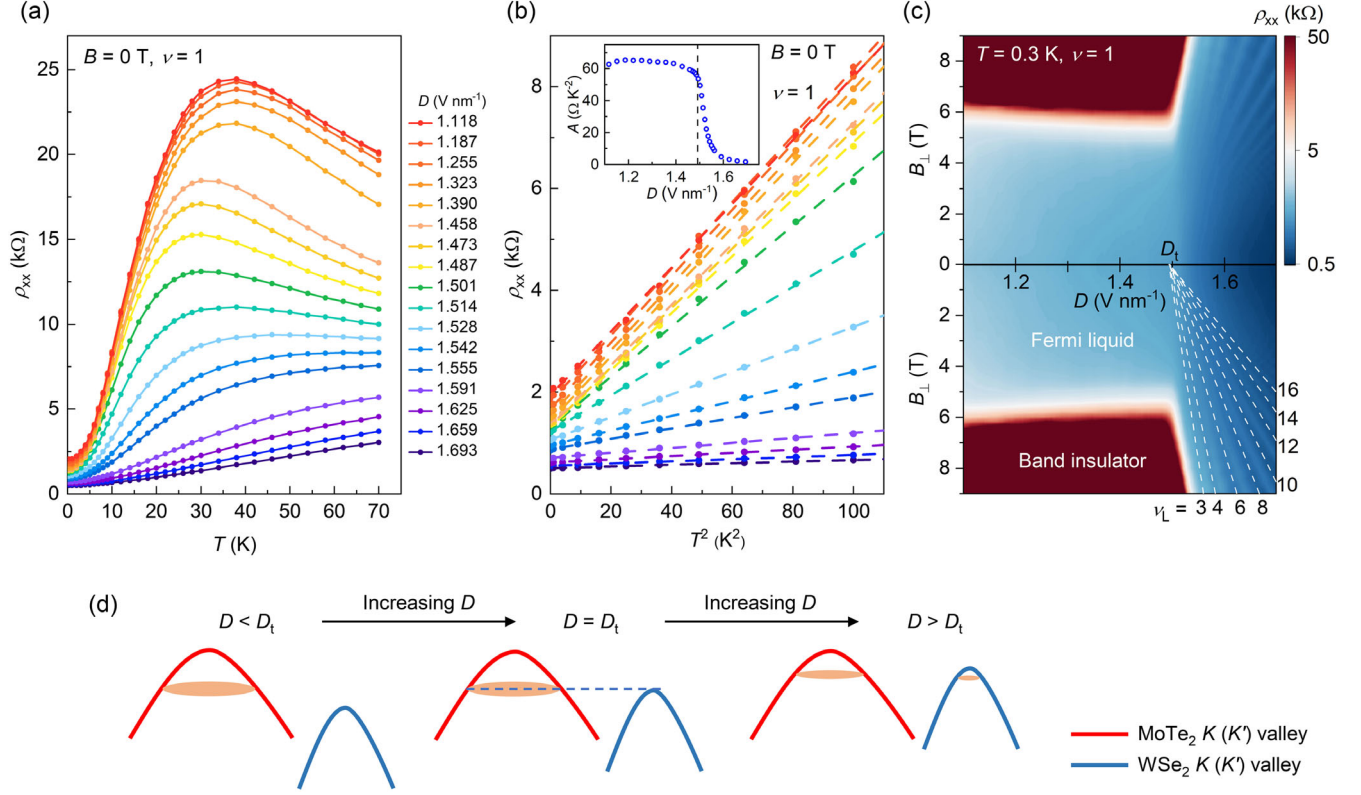


FIG. 2. Electric displacement field-driven Lifshitz transition. (a) Temperature dependences of ρ_{xx} with varying displacement field D at $\nu = 1$ and $B = 0$ T. (b) The same data as (a) (sharing the same color coding) with the x axis scaled in T^2 below about 10 K. The dashed lines are the corresponding linear fits. Inset: fitting parameter A as a function of D . The vertical dashed line indicates the inflection point at $D = D_t$. (c) The upper diagram shows ρ_{xx} as a function of out-of-plane magnetic field B_{\perp} and D at $\nu = 1$ and $T = 0.3$ K. The lower diagram shows color-coded regions representing different states. The Landau fan (linear dashed lines) converges to D_t , with filling factors ν_L labeled accordingly. (d) Schematics showing the Lifshitz transition and evolution of band alignments (K valleys of MoTe_2 and WSe_2) with increasing electric displacement field D . The K' valley is degenerate with the K valley at zero magnetic field and, hence, not drawn on this schematic. Various effects (such as moiré band formation and interaction-induced mass renormalization) are neglected in this simple schematic. Above D_t , charges are transferred between the MoTe_2 and the WSe_2 .

The hence enhanced charge localization is concomitant with an increase of entropy (per quasiparticle) toward $\ln 2$ (at approximately T^* , arising from the spin degree of freedom), whereas the Fermi-liquid state has a lower entropy proportional to T/T^* [55,56]. The contribution from the spin fluctuations to the entropy is shown later. At $T > \sim T^*$, the quasiparticle mean free path l becomes comparable to or smaller than the moiré wavelength of approximately 5 nm, and the transport enters an incoherent regime, giving rise to the insulating behavior. In the inset in Fig. 1(e), we plot the in-plane magnetic field (B_{\parallel}) dependences of ρ_{xx} at two different temperatures ($T = 1.6$ and 30 K). Unlike the TBG at $|\nu| = 1$ [52,53], 3L- $\text{MoTe}_2/\text{WSe}_2$ is insensitive to the in-plane magnetic field.

Now we discuss the effect of the vertical displacement field (D) at $\nu = 1$. At different temperatures, a similar value of the D field is observed where the resistance maxima disappear [Fig. 1(c)]. In Fig. 2(a), we plot the temperature dependence (0.3–70 K) of ρ_{xx} at different D fields. The ρ_{xx} gradually changes from a nonmonotonic behavior to a

monotonic and metallic behavior with a weaker T dependence at larger D fields. At low temperatures ($T < \sim 10$ K), all resistance curves follow T^2 dependences with $\rho_{xx}(T) = AT^2 + \rho_0$ [Fig. 2(b)]. The extracted A coefficient is plotted in the inset in Fig. 2(b) as a function of the D field. The A value stays nearly a constant at small D fields, while it decreases drastically by more than 30 folds starting from an inflection point at approximately 1.49 V nm^{-1} , which is denoted as the transition field D_t [dashed vertical line in the inset in Fig. 2(b)]. It indicates strong suppression of electronic interactions in the system and an approximately 80% reduction of effective quasiparticle mass. The high-temperature value of ρ_{xx} near D_t is close to 12.9 $\text{k}\Omega$. On both sides of the transition, the sample exhibits metallic ground states with Fermi liquid behaviors. This “metal-metal” transition observed here contrasts the electric-field-induced MIT found in $\text{MoTe}_2/\text{WSe}_2$ [38]. The D_t value (corresponding to $E_t = D_t/\epsilon_r = 0.50 \text{ V nm}^{-1}$, where ϵ_r is the out-of-plane dielectric constant of $h\text{-BN}$) is also smaller than the critical electric field (with $E_c = 0.65 \text{ V nm}^{-1}$) for MIT in the heterobilayer [38].

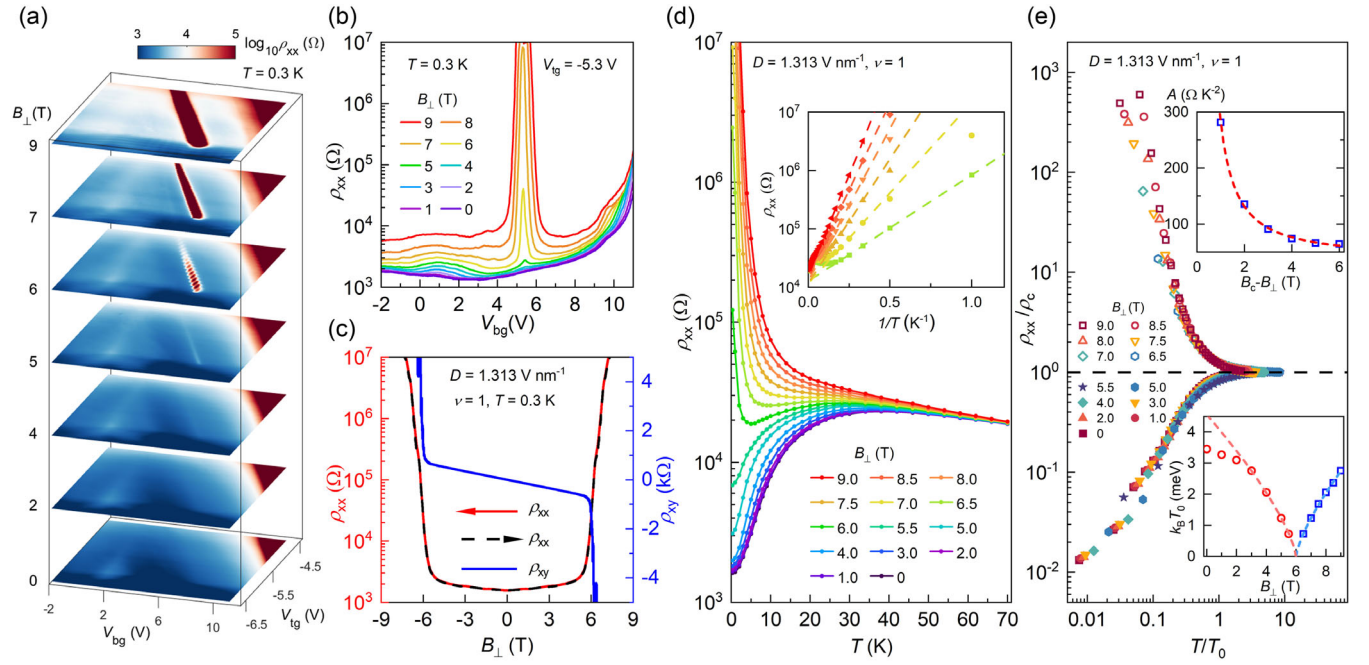


FIG. 3. Magnetic-field-induced metal-insulator transition. (a) Evolution of the insulating state at half filling as a function of out-of-plane magnetic field B_{\perp} . Each color plane shows the ρ_{xx} versus top and bottom gate voltages at a fixed B_{\perp} . (b) Showing V_{bg} sweeps of ρ_{xx} at a fixed $V_{tg} = -5.3$ V under varying B_{\perp} . Sharp resistance peaks occur at $\nu = 1$ above the critical magnetic field $B_c \approx 6$ T. (c) Red (dashed black) and blue curves show ρ_{xx} and ρ_{xy} as functions of B_{\perp} at 0.3 K, respectively. The gate voltages are fixed to ensure $\nu = 1$ and $D = 1.313$ V nm $^{-1}$, the same for (d) and (e). No hysteresis is observed upon sweeping down and up the magnetic fields (indicated by the red and dashed black arrows, respectively). (d) Temperature dependences of ρ_{xx} at different B_{\perp} , showing the magnetic-field-induced MIT. Inset: Dashed lines represent Arrhenius fits to extract activation gap magnitudes for $B_{\perp} > 6$ T. (e) Quantum critical scaling analysis of the MIT. The normalized resistance [by $\rho_c = \rho_{xx}(B = B_c)$] curves neatly collapse onto two branches that are almost “mirror symmetric,” with one showing an insulating behavior and the other showing a metallic behavior. The determination of the scaling temperature T_0 is discussed in the main text. Top inset: magnetic field dependence of A , where A is the fitting parameter for the low-temperature Fermi liquid. The dashed curve is a power-law fit $A^{1/2} \propto (B_c - B_{\perp})^{-0.98 \pm 0.11}$. Bottom inset: the scaling parameter $k_B T_0$ versus B_{\perp} on both sides of the critical field (red and blue open symbols). Close to B_c ($|B_{\perp} - B_c| \leq \sim 3$ T), both sides show power-law dependences with critical exponents 0.73 ± 0.02 (red and blue dashed curves).

The magnetotransport studies (under out-of-plane magnetic fields B_{\perp}) suggest that the D field in our sample introduces a Lifshitz transition at D_t , beyond which charges are redistributed between different subbands or layers. As shown in Fig. 2(c), the ρ_{xx} (at $\nu = 1$) is plotted as a function of both D and B_{\perp} at the base temperature $T = 0.3$ K. At small values of D , the sample encounters a transition to an insulating state (with $\rho_{xx} > 10^7$ Ω ; see more data in Fig. 3) above about 6 T. Combined with the barely changed in-plane magnetoresistance [inset in Fig. 1(e)], the strong magnetic anisotropy suggests an Ising type of spin-orbit coupling of the charge carriers that likely arise from K/K' valleys of the MoTe $_2$. It is also consistent with the fact that the finite out-of-plane displacement field lifts the layer degeneracy and leads to a strong localization of K/K' valley wave functions on the topmost layer of the trilayer MoTe $_2$ (more discussions can be found in Supplemental Material [51]) [62].

At larger values of D , clear Shubnikov–de Haas (SdH) oscillations due to the formation of Landau levels are

observed at $B_{\perp} > \sim 3$ T. The generated Landau fan (also indicated by the dashed lines in the lower diagram) converges to $D = 1.492$ V nm $^{-1}$ in the zero B_{\perp} field limit. The value coincides (while being more accurate) with the transition field D_t discussed above and indicates the emergence of a well-defined Fermi surface at $D > D_t$. Hence, it corresponds to a Lifshitz transition. The linear dependences of the Landau levels on the D field indicate that the size of the new Fermi surface is directly proportional to $(D - D_t)$. A cyclotron effective mass (0.52 ± 0.01) m_e (with m_e being the free electron mass) can be determined from analyzing the temperature dependence of the SdH oscillations (see more details in Supplemental Fig. S3 [51]). It is close to the effective mass found in monolayer WSe $_2$ K/K' valleys [63,64]. We, thus, conclude that the charge transfer induced by the vertical electric field happens between the K/K' valleys of the MoTe $_2$ top layer and the adjacent WSe $_2$ monolayer [schematics shown in Fig. 2(d)], giving rise to two sets of quantum oscillations observed at $D > D_t$ (see Supplemental

Fig. S4 [51]). Further evidence for assigning the valley occupations can be found in Supplemental Material [51]. Such observations place a question of explaining the electric-field-induced MIT as the bandwidth-controlled Mott transition within the framework of the single-band Hubbard model [38]. Since the charge transfer between MoTe₂ and WSe₂ can happen at rather low electric fields, another likely scenario is that the charge population in the WSe₂ layer naturally destroys the Mott insulating state in the heterobilayers. The Pomeranchuk effect observed near the critical electric field in the 1L-MoTe₂/WSe₂, hence, may have a very different origin comparing to our observations in a relatively large electric field range ($1.1 \text{ V nm}^{-1} < D < D_t$) where the single-band Hubbard model description is valid.

In the following, we demonstrate the quantum criticality induced by the out-of-plane magnetic field B_{\perp} at $\nu = 1$ and $D < D_t$. We plot the dual-gate mappings of ρ_{xx} at different B_{\perp} [Fig. 3(a)]. A resistance peak at $\nu = 1$ can be identified at approximately 5 T for $D < D_t$ and quickly becomes prominent at higher fields [see line cuts in Fig. 3(b)]. At fixed D fields [see an example in Fig. 3(c)], the ρ_{xx} weakly depends on B_{\perp} at low magnetic fields, accompanied by a linear Hall resistance ρ_{xy} due to the Lorentz force. The low-field Hall slope gives a density of $5.4 \times 10^{12} \text{ cm}^{-2}$, close to the expected moiré density. Both ρ_{xx} and ρ_{xy} diverge at approximately 6 T, which is then identified as the critical magnetic field B_c . The B_{\perp} -induced MIT at $\nu = 1$ is clearly illustrated in Fig. 3(d), where we show the temperature dependences of sheet resistance ρ_{xx} (0.3–70 K) at a few representative magnetic fields. Above B_c , the sample exhibits characteristics of an insulator following a thermal activation behavior $\rho_{xx} \propto E^{(\Delta/2k_B T)}$ [inset in Fig. 3(d)], where k_B is the Boltzmann constant and Δ is the activation gap. At low temperatures and below the critical field (B_c), the resistance drops upon cooling, exhibiting the characteristics of Fermi liquids. The extracted prefactor A is plotted as a function of $|B_{\perp} - B_c|$ in the upper inset in Fig. 3(e), showing a power-law dependence $A^{1/2} \propto (B_c - B_{\perp})^{-0.98 \pm 0.11}$. Our result suggests a divergence of the effective mass ($\propto A^{1/2}$) at the MIT [65,66]. After normalizing $\rho_{xx}(T)$ by the $\rho_c(T)$ at 6 T (critical field B_c) and scaling the temperature by a field-dependent T_0 , the resistance curves readily collapse onto two branches in the Fig. 3(e) log-log plot. We notice the ρ_c has a complicated dependence on the temperature. Possible reasons are discussed in Supplemental Material [51]. On the insulating side ($B_{\perp} > B_c$), T_0 is calculated from the fitting parameter Δ/k_B , while on the metallic side ($B_{\perp} < B_c$), the same T_0 is used as the insulating side with equal distance to the critical field at $|B_{\perp} - B_c| \leq 3 \text{ T}$. Because we do not have data at higher magnetic fields, the T_0 's of $B_{\perp} = 0$ –2 T are picked independently to scale the curves nearly symmetric to the insulating branches about $\rho_{xx}/\rho_c = 1$. The scaling parameter $k_B T_0$ continuously vanishes as it approaches the critical field [lower inset in

Fig. 3(e)]. The B_{\perp} dependences of $k_B T_0$ follow a power-law behavior $k_B T_0 \propto |B_{\perp} - B_c|^{0.73 \pm 0.02}$ near both sides of the critical field (highlighted by the dashed red and blue curves, respectively). The critical exponent 0.73 ± 0.02 is close to the value found in the bandwidth-tuned MIT reported by Li *et al.* [38], indicating the QPTs tuned by the two different parameters share the same universality class. The half-filled Hubbard model under an external magnetic field has been extensively studied theoretically [44–47,67]. It has been puzzling for a long time whether the magnetic-field-driven MIT should be continuous or first-order-like. Recent studies suggest the nature of the transition depends on the correlation strength. Our observation in 3L-MoTe₂/WSe₂ near the critical field (with strongly enhanced effective masses when approaching the transition from the metallic side) is, in general, consistent with the theoretical prediction of the magnetic-field-induced spin-polarized band insulator at the intermediate correlation strength ($U \sim W$) [44,46,47]. However, we do not observe any hysteresis upon sweeping up and down the magnetic field [Fig. 3(c)], signifying the character of a continuous phase transition. We can then estimate the Zeeman energy $g\mu_B B_{\perp} \sim W^* \sim k_B T^*$ to be 3.5 meV and the Landé g factor to be $g \sim 10$. The role of orbital effects from the out-of-plane magnetic fields that could reduce the bandwidth is not considered here.

IV. DISCUSSION AND CONCLUSION

Figure 4 summarizes our main observations at half filling of the 3L-MoTe₂/WSe₂ sample. In Fig. 4(a), the resistance (in logarithmic scale) is plotted in the three-dimensional space projected on the $T - D$ ($B_{\perp} = 0$), $T - B_{\perp}$ ($D = 1.313 \text{ V nm}^{-1}$), and $D - B_{\perp}$ ($T = 0.3 \text{ K}$) planes. The temperature and magnetic field axes are drawn as $k_B T$ and $g\mu_B B_{\perp}$ to represent the thermal and Zeeman energies, respectively. First, the vertical electric field can induce charge transfer between different subbands and cause a breakdown of the single-band description of the system. It drives the system from a strongly interacting metal to a weakly interacting metal (evidenced by the great reduction of the A value) accompanied by the Lifshitz transition. Second, the perpendicular magnetic field induces the metal-to-insulator QPT at B_c (highlighted by the dashed yellow curve in the $D - B_{\perp}$ plane). The asterisk symbols illustrate the T^* (separating the high-temperature insulating behavior from the low-temperature Fermi liquids) as a function of D and B_{\perp} . A quantum tricritical point (highlighted by the pink circle) can be identified at $D_t = 1.49 \text{ V nm}^{-1}$ and $B_c = \sim 6 \text{ T}$ where phase transitions tuned by the two nearly independent parameters meet at the base temperature (see more discussions in Supplemental Fig. S4 [51]).

In Fig. 4(b), we illustrate the generally accepted phase diagram of the half-filled triangular lattice Hubbard model with tuning the interaction strength U/W . The ground state

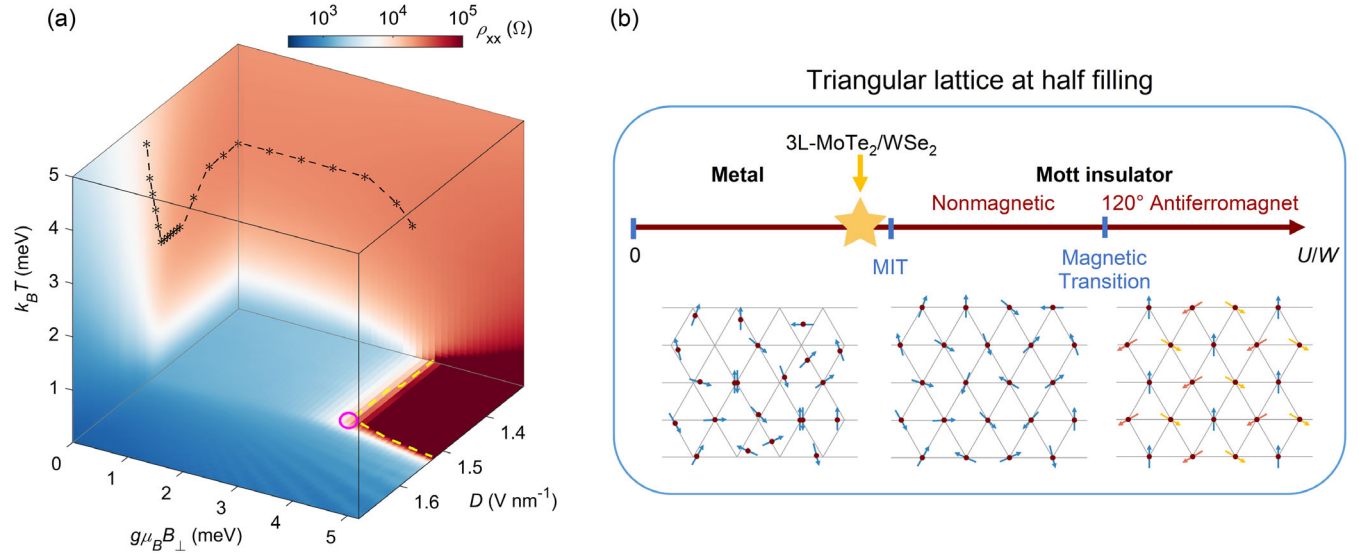


FIG. 4. Phase diagram of 3L-MoTe₂/WSe₂ at half filling. (a) Longitudinal resistivity ρ_{xx} (in log scale) as a function of $g\mu_B B_{\perp}$, D , and $k_B T$. The diagram shows three slices of the function. Different states can be identified by the color contrast. The low-field light blue area denotes the Fermi liquid phase; the dark red area denotes the magnetic-field-induced insulating phase. Lifshitz transition occurs near 1.5 V nm^{-1} and generates a dark blue area at large D . In the dark blue area at the base temperature, Landau fan can be observed. The pink circle, the asterisk symbols, and the dashed yellow curves highlight the tricritical point in the $g\mu_B B_{\perp} - D$ plane, the coherent-incoherent transport crossover temperature T^* , and critical field B_c , respectively. (b) The expected phase diagram of the triangular lattice Hubbard model. Our 3L-MoTe₂/WSe₂ lies on the left boundary of the MIT (denoted by the yellow arrow and star). Lower-panel schematics show the real-space charge distributions and spin orientations (denoted by the arrows) for corresponding phases. The metal and nonmagnetic insulator phases have random spin orientations, while the system favors 120° Néel order in the large U/W limit.

of our sample at $D < D_t$ and $B_{\perp} = 0$ is a correlated metal exhibiting a Fermi-liquid behavior at low temperatures (with strongly renormalized effective mass) and Pomeranchuk effects. The observations are consistent with an intermediate coupling strength in the vicinity to the left side of the MIT [32,37,55,56] [marked by the yellow star in Fig. 4(b)]. Spin fluctuations and geometric frustrations give rise to larger entropy in the exotic nonmagnetic insulating state (e.g., chiral QSLs [36,37]) compared with the metal phase. Pomeranchuk effect arises with the enhanced charge localization at higher temperatures, since it yields a gain in free energy. It can also be seen from the Maxwell relation

$$\left. \frac{\partial S}{\partial U} \right|_T = - \left. \frac{\partial F}{\partial T} \right|_U,$$

where double occupancy (F denoting the fraction of the charges in doubly occupied lattice sites) decreases (namely, single occupancy increases) as a function of the temperature, since the entropy S is positively correlated with U near the MIT [37,55,68]. The perpendicular magnetic-field-driven MIT likely originates from the Zeeman-field-induced spin splitting, realizing a spin-polarized band insulator at high fields (when the Zeeman energy exceeds the renormalized bandwidth W^*) [44–47].

The vicinity to the intermediate coupling region in 3L-MoTe₂/WSe₂ provides a novel example of the richness and complex phase diagrams that can be unveiled in moiré superlattices. The observed Pomeranchuk effect is closely related to the higher entropy in the singly occupied state at half filling. Our observations could have implications on the existence of the elusive QSL phase at larger correlation strength, whereas compelling evidence is still missing. The multiband nature of the system also suggests it as a promising platform to construct and simulate the physics of a two-band Hubbard model [11] or a moiré Kondo lattice [69,70] with unprecedented controllability.

ACKNOWLEDGMENTS

The authors thank Professor Kin Fai Mak and Professor Cenke Xu for valuable discussions. This work was primarily funded by the National Key R&D Program of China (Grant No. 2021YFA1401300). Support was also provided by the National Natural Science Foundation of China (Grants No. 12174439 and No. 12074375) and the Strategic Priority Research Program of Chinese Academy of Sciences (Grants No. XDB28000000 and No. XDB33000000). The growth of h -BN crystals was supported by the Elemental Strategy Initiative of MEXT, Japan, and CREST (JPMJCR15F3), JST.

- [1] Y. Cao, V. Fatemi, A. Demir, S. Fang, S. L. Tomarken, J. Y. Luo, J. D. Sanchez-Yamagishi, K. Watanabe, T. Taniguchi, E. Kaxiras *et al.*, *Correlated Insulator Behaviour at Half-Filling in Magic-Angle Graphene Superlattices*, *Nature (London)* **556**, 80 (2018).
- [2] Y. Cao, V. Fatemi, S. Fang, K. Watanabe, T. Taniguchi, E. Kaxiras, and P. Jarillo-Herrero, *Unconventional Superconductivity in Magic-Angle Graphene Superlattices*, *Nature (London)* **556**, 43 (2018).
- [3] L. Balents, C. R. Dean, D. K. Efetov, and A. F. Young, *Superconductivity and Strong Correlations in Moiré Flat Bands*, *Nat. Phys.* **16**, 725 (2020).
- [4] E. Y. Andrei, D. K. Efetov, P. Jarillo-Herrero, A. H. MacDonald, K. F. Mak, T. Senthil, E. Tutuc, A. Yazdani, and A. F. Young, *The Marvels of Moiré Materials*, *Nat. Rev. Mater.* **6**, 201 (2021).
- [5] F. Wu, T. Lovorn, E. Tutuc, and A. H. MacDonald, *Hubbard Model Physics in Transition Metal Dichalcogenide Moiré Bands*, *Phys. Rev. Lett.* **121**, 026402 (2018).
- [6] F. Wu, T. Lovorn, E. Tutuc, I. Martin, and A. H. MacDonald, *Topological Insulators in Twisted Transition Metal Dichalcogenide Homobilayers*, *Phys. Rev. Lett.* **122**, 086402 (2019).
- [7] K. Slagle and L. Fu, *Charge Transfer Excitations, Pair Density Waves, and Superconductivity in Moiré Materials*, *Phys. Rev. B* **102**, 235423 (2020).
- [8] Y. Zhang, T. Liu, and L. Fu, *Electronic Structures, Charge Transfer, and Charge Order in Twisted Transition Metal Dichalcogenide Bilayers*, *Phys. Rev. B* **103**, 155142 (2021).
- [9] T. Devakul, V. Crépel, Y. Zhang, and L. Fu, *Magic in Twisted Transition Metal Dichalcogenide Bilayers*, *Nat. Commun.* **12**, 6730 (2021).
- [10] Y.-T. Hsu, F. Wu, and S. Das Sarma, *Spin-Valley Locked Instabilities in Moiré Transition Metal Dichalcogenides with Conventional and Higher-Order van Hove Singularities*, *Phys. Rev. B* **104**, 195134 (2021).
- [11] Y.-H. Zhang, D. N. Sheng, and A. Vishwanath, *SU(4) Chiral Spin Liquid, Exciton Supersolid, and Electric Detection in Moiré Bilayers*, *Phys. Rev. Lett.* **127**, 247701 (2021).
- [12] H. Pan and S. Das Sarma, *Interaction Range and Temperature Dependence of Symmetry Breaking in Strongly Correlated Two-Dimensional Moiré Transition Metal Dichalcogenide Bilayers*, *Phys. Rev. B* **105**, 041109 (2022).
- [13] M. Biderang, M.-H. Zare, and J. Sirker, *Proximity-Driven Ferromagnetism and Superconductivity in the Triangular Rashba-Hubbard Model*, *Phys. Rev. B* **105**, 064504 (2022).
- [14] Z. Zhu, D. N. Sheng, and A. Vishwanath, *Doped Mott Insulators in the Triangular-Lattice Hubbard Model*, *Phys. Rev. B* **105**, 205110 (2022).
- [15] K. F. Mak and J. Shan, *Semiconductor Moiré Materials*, *Nat. Nanotechnol.* **17**, 686 (2022).
- [16] E. M. Alexeev, D. A. Ruiz-Tijerina, M. Danovich, M. J. Hamer, D. J. Terry, P. K. Nayak, S. Ahn, S. Pak, J. Lee, J. I. Sohn *et al.*, *Resonantly Hybridized Excitons in Moiré Superlattices in van der Waals Heterostructures*, *Nature (London)* **567**, 81 (2019).
- [17] C. Jin, E. C. Regan, A. Yan, M. Iqbal Bakti Utama, D. Wang, S. Zhao, Y. Qin, S. Yang, Z. Zheng, S. Shi *et al.*, *Observation of Moiré Excitons in WSe₂/WS₂ Heterostructure Superlattices*, *Nature (London)* **567**, 76 (2019).
- [18] K. L. Seyler, P. Rivera, H. Yu, N. P. Wilson, E. L. Ray, D. G. Mandrus, J. Yan, W. Yao, and X. Xu, *Signatures of Moiré-Trapped Valley Excitons in MoSe₂/WSe₂ Heterobilayers*, *Nature (London)* **567**, 66 (2019).
- [19] K. Tran, G. Moody, F. Wu, X. Lu, J. Choi, K. Kim, A. Rai, D. A. Sanchez, J. Quan, A. Singh *et al.*, *Evidence for Moiré Excitons in van der Waals Heterostructures*, *Nature (London)* **567**, 71 (2019).
- [20] E. Liu, E. Barré, J. van Baren, M. Wilson, T. Taniguchi, K. Watanabe, Y.-T. Cui, N. M. Gabor, T. F. Heinz, Y.-C. Chang *et al.*, *Signatures of Moiré Trions in WSe₂/MoSe₂ Heterobilayers*, *Nature (London)* **594**, 46 (2021).
- [21] X. Wang, J. Zhu, K. L. Seyler, P. Rivera, H. Zheng, Y. Wang, M. He, T. Taniguchi, K. Watanabe, J. Yan *et al.*, *Moiré Trions in MoSe₂/WSe₂ Heterobilayers*, *Nat. Nanotechnol.* **16**, 1208 (2021).
- [22] L. Zhang, F. Wu, S. Hou, Z. Zhang, Y.-H. Chou, K. Watanabe, T. Taniguchi, S. R. Forrest, and H. Deng, *van der Waals Heterostructure Polaritons with Moiré-Induced Nonlinearity*, *Nature (London)* **591**, 61 (2021).
- [23] Y. Tang, L. Li, T. Li, Y. Xu, S. Liu, K. Barmak, K. Watanabe, T. Taniguchi, A. H. MacDonald, J. Shan *et al.*, *Simulation of Hubbard Model Physics in WSe₂/WS₂ Moiré Superlattices*, *Nature (London)* **579**, 353 (2020).
- [24] L. Wang, E.-M. Shih, A. Ghiotto, L. Xian, D. A. Rhodes, C. Tan, M. Claassen, D. M. Kennes, Y. Bai, B. Kim *et al.*, *Correlated Electronic Phases in Twisted Bilayer Transition Metal Dichalcogenides*, *Nat. Mater.* **19**, 861 (2020).
- [25] Y. Shimazaki, I. Schwartz, K. Watanabe, T. Taniguchi, M. Kroner, and A. Imamoğlu, *Strongly Correlated Electrons and Hybrid Excitons in a Moiré Heterostructure*, *Nature (London)* **580**, 472 (2020).
- [26] E. C. Regan, D. Wang, C. Jin, M. I. Bakti Utama, B. Gao, X. Wei, S. Zhao, W. Zhao, Z. Zhang, K. Yumigeta *et al.*, *Mott and Generalized Wigner Crystal States in WSe₂/WS₂ Moiré Superlattices*, *Nature (London)* **579**, 359 (2020).
- [27] Y. Xu, S. Liu, D. A. Rhodes, K. Watanabe, T. Taniguchi, J. Hone, V. Elser, K. F. Mak, and J. Shan, *Correlated Insulating States at Fractional Fillings of Moiré Superlattices*, *Nature (London)* **587**, 214 (2020).
- [28] X. Huang, T. Wang, S. Miao, C. Wang, Z. Li, Z. Lian, T. Taniguchi, K. Watanabe, S. Okamoto, D. Xiao *et al.*, *Correlated Insulating States at Fractional Fillings of the WS₂/WSe₂ Moiré Lattice*, *Nat. Phys.* **17**, 715 (2021).
- [29] C. Jin, Z. Tao, T. Li, Y. Xu, Y. Tang, J. Zhu, S. Liu, K. Watanabe, T. Taniguchi, J. C. Hone *et al.*, *Stripe Phases in WSe₂/WS₂ Moiré Superlattices*, *Nat. Mater.* **20**, 940 (2021).
- [30] H. Li, S. Li, E. C. Regan, D. Wang, W. Zhao, S. Kahn, K. Yumigeta, M. Blei, T. Taniguchi, K. Watanabe *et al.*, *Imaging Two-Dimensional Generalized Wigner Crystals*, *Nature (London)* **597**, 650 (2021).
- [31] T. Li, S. Jiang, B. Shen, Y. Zhang, L. Li, Z. Tao, T. Devakul, K. Watanabe, T. Taniguchi, L. Fu, J. Shan, and K. F. Mak, *Quantum Anomalous Hall Effect from Intertwined Moiré Bands*, *Nature (London)* **600**, 641 (2021).
- [32] K. Aryanpour, W. E. Pickett, and R. T. Scalettar, *Dynamical Mean-Field Study of the Mott Transition in the Half-Filled*

- Hubbard Model on a Triangular Lattice*, *Phys. Rev. B* **74**, 085117 (2006).
- [33] T. Yoshioka, A. Koga, and N. Kawakami, *Quantum Phase Transitions in the Hubbard Model on a Triangular Lattice*, *Phys. Rev. Lett.* **103**, 036401 (2009).
- [34] H.-Y. Yang, A. M. Läuchli, F. Mila, and K. P. Schmidt, *Effective Spin Model for the Spin-Liquid Phase of the Hubbard Model on the Triangular Lattice*, *Phys. Rev. Lett.* **105**, 267204 (2010).
- [35] T. Shirakawa, T. Tohyama, J. Kokalj, S. Sota, and S. Yunoki, *Ground-State Phase Diagram of the Triangular Lattice Hubbard Model by the Density-Matrix Renormalization Group Method*, *Phys. Rev. B* **96**, 205130 (2017).
- [36] A. Szasz, J. Motruk, M. P. Zaletel, and J. E. Moore, *Chiral Spin Liquid Phase of the Triangular Lattice Hubbard Model: A Density Matrix Renormalization Group Study*, *Phys. Rev. X* **10**, 021042 (2020).
- [37] A. Wietek, R. Rossi, F. Šimkovic IV, M. Klett, P. Hansmann, M. Ferrero, E. M. Stoudenmire, T. Schäfer, and A. Georges, *Mott Insulating States with Competing Orders in the Triangular Lattice Hubbard Model*, *Phys. Rev. X* **11**, 041013 (2021).
- [38] T. Li, S. Jiang, L. Li, Y. Zhang, K. Kang, J. Zhu, K. Watanabe, T. Taniguchi, D. Chowdhury, L. Fu *et al.*, *Continuous Mott Transition in Semiconductor Moiré Superlattices*, *Nature (London)* **597**, 350 (2021).
- [39] A. Ghiotto, E.-M. Shih, G. S. Pereira, D. A. Rhodes, B. Kim, J. Zang, A. J. Millis, K. Watanabe, T. Taniguchi, J. C. Hone *et al.*, *Quantum Criticality in Twisted Transition Metal Dichalcogenides*, *Nature (London)* **597**, 345 (2021).
- [40] S. Ahn and S. Das Sarma, *Disorder-Induced Two-Dimensional Metal-Insulator Transition in Moiré Transition Metal Dichalcogenide Multilayers*, *Phys. Rev. B* **105**, 115114 (2022).
- [41] J. Zang, J. Wang, J. Cano, A. Georges, and A. J. Millis, *Dynamical Mean-Field Theory of Moiré Bilayer Transition Metal Dichalcogenides: Phase Diagram, Resistivity, and Quantum Criticality*, *Phys. Rev. X* **12**, 021064 (2022).
- [42] Y. Xu, X.-C. Wu, M. Ye, Z.-X. Luo, C.-M. Jian, and C. Xu, *Interaction-Driven Metal-Insulator Transition with Charge Fractionalization*, *Phys. Rev. X* **12**, 021067 (2022).
- [43] D. C. Sunghoon Kim and T. Senthil, *Continuous Mott Transition in Moiré Semiconductors: Role of Long-Wavelength Inhomogeneities*, [arXiv:2204.10865v1](https://arxiv.org/abs/2204.10865v1).
- [44] L. Laloux, A. Georges, and W. Krauth, *Effect of a Magnetic Field on Mott-Hubbard Systems*, *Phys. Rev. B* **50**, 3092 (1994).
- [45] J. Bauer and A. C. Hewson, *Field-Dependent Quasiparticles in the Infinite-Dimensional Hubbard Model*, *Phys. Rev. B* **76**, 035118 (2007).
- [46] M. M. Wysokiński and J. Spałek, *Properties of an Almost Localized Fermi Liquid in an Applied Magnetic Field Revisited: A Statistically Consistent Gutzwiller Approach*, *J. Phys. Condens. Matter* **26**, 055601 (2014).
- [47] W. Zhu, D. N. Sheng, and J.-X. Zhu, *Magnetic Field Dependent Dynamics and Field-Driven Metal-to-Insulator Transition of the Half-Filled Hubbard Model: A DMFT + DMRG Study*, *Phys. Rev. B* **96**, 085118 (2017).
- [48] Z. Zhan, Y. Zhang, P. Lv, H. Zhong, G. Yu, F. Guinea, J. A. Silva-Guillén, and S. Yuan, *Tunability of Multiple Ultraflat Bands and Effect of Spin-Orbit Coupling in Twisted Bilayer Transition Metal Dichalcogenides*, *Phys. Rev. B* **102**, 241106(R) (2020).
- [49] M. Angeli and A. H. MacDonald, *Γ Valley Transition Metal Dichalcogenide Moiré Bands*, *Proc. Natl. Acad. Sci. U.S.A.* **118**, e2021826118 (2021).
- [50] L. Xian, M. Claassen, D. Kiese, M. M. Scherer, S. Trebst, D. M. Kennes, and A. Rubio, *Realization of Nearly Dispersionless Bands with Strong Orbital Anisotropy from Destructive Interference in Twisted Bilayer MoS₂*, *Nat. Commun.* **12**, 5644 (2021).
- [51] See Supplemental Material at <http://link.aps.org/supplemental/10.1103/PhysRevX.12.041015> for details of sample fabrication, band structure analyses, and more supplemental data.
- [52] A. Rozen, J. M. Park, U. Zondiner, Y. Cao, D. Rodan-Legrain, T. Taniguchi, K. Watanabe, Y. Oreg, A. Stern, E. Berg *et al.*, *Entropic Evidence for a Pomeranchuk Effect in Magic-Angle Graphene*, *Nature (London)* **592**, 214 (2021).
- [53] Y. Saito, F. Yang, J. Ge, X. Liu, T. Taniguchi, K. Watanabe, J. Li, E. Berg, and A. F. Young, *Isospin Pomeranchuk Effect in Twisted Bilayer Graphene*, *Nature (London)* **592**, 220 (2021).
- [54] R. C. Richardson, *The Pomeranchuk Effect*, *Rev. Mod. Phys.* **69**, 683 (1997).
- [55] A. Georges and W. Krauth, *Numerical Solution of the $d = \infty$ Hubbard Model: Evidence for a Mott Transition*, *Phys. Rev. Lett.* **69**, 1240 (1992).
- [56] A. Georges and W. Krauth, *Physical Properties of the Half-Filled Hubbard Model in Infinite Dimensions*, *Phys. Rev. B* **48**, 7167 (1993).
- [57] M. Rice, *Electron-Electron Scattering in Transition Metals*, *Phys. Rev. Lett.* **20**, 1439 (1968).
- [58] K. Kadowaki and S. Woods, *Universal Relationship of the Resistivity and Specific Heat in Heavy-Fermion Compounds*, *Solid State Commun.* **58**, 507 (1986).
- [59] A. Jacko, J. Fjærestad, and B. Powell, *A Unified Explanation of the Kadowaki-Woods Ratio in Strongly Correlated Metals*, *Nat. Phys.* **5**, 422 (2009).
- [60] M. M. Radonjić, D. Tanasković, V. Dobrosavljević, K. Haule, and G. Kotliar, *Wigner-Mott Scaling of Transport near the Two-Dimensional Metal-Insulator Transition*, *Phys. Rev. B* **85**, 085133 (2012).
- [61] E. Pavarini, P. Coleman, and E. Koch, *Many-Body Physics: From Kondo to Hubbard. Heavy Fermions and the Kondo Lattice: A 21st Century Perspective* (Forschungszentrum Jülich, Jülich, 2015).
- [62] H. C. P. Movva, T. Lovorn, B. Fallahazad, S. Larentis, K. Kim, T. Taniguchi, K. Watanabe, S. K. Banerjee, A. H. MacDonald, and E. Tutuc, *Tunable Γ -K Valley Populations in Hole-Doped Trilayer WSe₂*, *Phys. Rev. Lett.* **120**, 107703 (2018).
- [63] H. C. P. Movva, B. Fallahazad, K. Kim, S. Larentis, T. Taniguchi, K. Watanabe, S. K. Banerjee, and E. Tutuc, *Density-Dependent Quantum Hall States and Zeeman Splitting in Monolayer and Bilayer WSe₂*, *Phys. Rev. Lett.* **118**, 247701 (2017).
- [64] M. V. Gustafsson, M. Yankowitz, C. Forsythe, D. Rhodes, K. Watanabe, T. Taniguchi, J. Hone, X. Zhu, and C. R.

- Dean, *Ambipolar Landau Levels and Strong Band-Selective Carrier Interactions in Monolayer WSe₂*, *Nat. Mater.* **17**, 411 (2018).
- [65] V. Dobrosavljevic, N. Trivedi, and J.M. Valles, Jr., *Conductor-Insulator Quantum Phase Transitions* (Oxford University, New York, 2012).
- [66] T. Senthil, *Theory of a Continuous Mott Transition in Two Dimensions*, *Phys. Rev. B* **78**, 045109 (2008).
- [67] S. Acheche, L.-F. Arsenault, and A. M. S. Tremblay, *Orbital Effect of the Magnetic Field in Dynamical Mean-Field Theory*, *Phys. Rev. B* **96**, 235135 (2017).
- [68] F. Werner, O. Parcollet, A. Georges, and S.R. Hassan, *Interaction-Induced Adiabatic Cooling and Antiferromagnetism of Cold Fermions in Optical Lattices*, *Phys. Rev. Lett.* **95**, 056401 (2005).
- [69] A. Kumar, N. C. Hu, A. H. MacDonald, and A. C. Potter, *Gate-Tunable Heavy Fermion Quantum Criticality in a Moiré Kondo Lattice*, *Phys. Rev. B* **106**, L041116 (2022).
- [70] A. Dalal and J. Ruhman, *Orbitally Selective Mott Phase in Electron-Doped Twisted Transition Metal-Dichalcogenides: A Possible Realization of the Kondo Lattice Model*, *Phys. Rev. Res.* **3**, 043173 (2021).